arXiv:1211.5444v1 [cond-mat.mes-hall] 23 Nov 2012

Landau levels, edge states and magneto-conductance in GaAs/AlGaAs core-shell nanowires

Miquel Royo* and Andrea Bertoni†
CNR-NANO S3, Institute for Nanoscience,
Via Campi 213/a, 41125 Modena, Italy

Guido Goldoni‡
Department of Physics, Informatics and Mathematics,
University of Modena and Reggio Emilia, Italy and
CNR-NANO S3, Institute for Nanoscience,
Via Campi 213/a, 41125 Modena, Italy

(Dated: November 26, 2012)

Abstract

Magnetic states of the electron gas confined in core-shell nanowires are calculated in a mean-field self-consistent approach for a transverse field of arbitrary strength and orientation, and magneto-conductance is predicted within a Landauer approach. Calculations have been performed including radial modulation of realistic GaAs/AlGaAs devices with prismatic symmetry, at different doping and charge density regimes. Magnetic states in the Quantum Hall regime can partially be described in terms of Landau levels and edge states, familiar from two-dimensional electron gases. However, particularly at high free charge density, where the dominating electron-electron interaction leads to strongly inhomogeneous localization, the magnetic field competes with the electrostatic potential, resulting in complex dispersions and negative magneto-resistance. In the high density regime the marked magnetic anisotropy of the magneto-conductance is a direct probe of the inhomogeneous electron gas localization induced by the prismatic geometry.

PACS numbers: 73.21.Hb, 73.43.Cd, 73.63.Nm, 75.75.-c, 03.65.Ge

I. INTRODUCTION

Radially modulated semiconductor heterostructures, realized from core-(multi)shell nanowires (CSNWs),[1–5] offer new perspectives in quantum electronics.[6] Several crucial steps have been taken toward the realization of high-mobility devices based on this new class of nano-materials and their integration.[7] Single-crystal, defect-free cores using several III-V's,[8,9] selective *radial* doping,[10] high quality interfaces,[11] and integration with Si substrates[12] have been realized.

Figure 1 show the schematics of a radial heterojunction in GaAs/AlGaAs. A GaAs nanowire, which typically grows along the [111] direction radially exposing the six $\{110\}$ facets, is epitaxially overgrown by an AlGaAs shell,[13] including a doping layer,[14] and a GaAs capping layer, which protects the AlGaAs layer from oxidation.[15] Surface states of the GaAs capping layer, which are about the midgap energy, easily deplete the outer layers of the structure, and an electron gas may form at the inner GaAs/AlGaAs hetero-interface.[4]

Such a radial modulation doped heterojunction is a candidate for hosting a high-mobility electron gas with a novel prismatic shape, adding to high-mobility two-dimensional electron gases (2DEGs) that exposed a wealth of new fundamental physics and innovative applications. One might think to such a system as a wrapped 2DEG at the inner GaAs/AlGaAs heterointerface. However, due to the prismatic shape of the core and to electron-electron interaction, in a CSNW channel the electron gas will not be uniformly distributed at the heterointerfaces. Mean-field calculations[16,17] for radial heterojunctions at zero magnetic field show that the electron gas distribution strongly depends on the free charge density.[12] We have previously identified[16] three regimes for conduction electrons in GaAs (holes, as shown in Ref. 16, may assume substantially different distribution, but they will not be considered in this paper): i) a low density regime, with the electron gas cylindrically distributed in a quasi-1D channel deep into the GaAs core; ii) an intermediate density regime, where the central region of the core is depleted and the electron gas shapes itself in a broad cylindrical distribution; iii) a high density regime in which the electron gas separates itself in a set of quasi-1D channels, strongly tunnel coupled, and concentrated at the edges between different facets of the hexagonal core, to maximize the inter-electron distance. Conductive channels in CSNWs are very sensitive to an external field and may be reshaped by an external wrap-around gate, an important aspect, e.g., for FET design.[12]

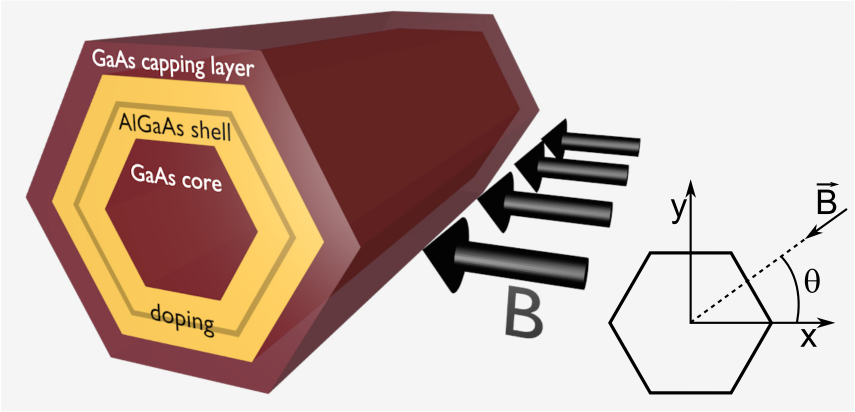

FIG. 1. Schematics of the prototypical radial heterojunction studied in this work. Remote doping in the middle of the AlGaAs layer results in an electron gas at the inner GaAs/AlGaAs interface. A transverse uniform magnetic field is applied. Inset: axis definitions and angle θ formed by the magnetic field.

Size and shape of conductive channels with confinement length in the tens of nanometers range may be directly probed by an external magnetic field, thanks to the competition between electrostatic confinement and the tunable magnetic length. Magnetic states in models of CSNWs have been first addressed in Ref. 18, where confinement on a prismatic surface has been *assumed*, showing that a transverse magnetic field competes with preferential localization at the edges between facets, enhancing or depleting these quasi-1D channels, depending on the field orientation with respect to the nanowire facets. The model used, however, does not apply closely to a doped heterojuction, as carrier-carrier interaction was neglected. On the other hand, no magneto-transport experiment in the Quantum Hall regime in CSNWs is available to date.

In this paper, we report self-consistent field calculations of realistic CSNWs subjected to a transverse magnetic field in the Quantum Hall regime. Our target systems are remotely doped GaAs/AlGaAs radial single heterojunctions. Energy subbands and charge densities are calculated at different regimes with strong fields of different orientations. Calculations show that magnetic fields shape the electronic states, which can partially be described in terms of Landau levels (LLs) and edge states (ESs). However, at high density the strong electron-electron interaction leads to strongly inhomogeneous localization of the electron gas, which, in turn, reflects in a region of anisotropic, negative magneto-resistance.

II. METHOD

Within the effective mass, single parabolic band approximation, the Hamiltonian in an external magnetic field reads

$$\hat{H} = \frac{1}{2}\left(\hat{P} - e\,A(\mathbf{R})\right)\frac{1}{m^*(\mathbf{R})}\left(\hat{P} - e\,A(\mathbf{R})\right) + E_C(\mathbf{R}) - e\,V(\mathbf{R}). \tag{1}$$

where $\mathbf{R} = (x, y, z)$, $\hat{P}$ is the conjugate momentum operator, $A(\mathbf{R})$ is the magnetic vector potential, and $m^*(\mathbf{R})$ is the position dependent, isotropic electron effective mass. $E_C(\mathbf{r})$ and $V(\mathbf{r})$ are, respectively, the local conduction band edge and the self-consistent potential generated by other electrons and the fully-ionized, static donors.

To describe a transverse magnetic field, namely, perpendicular to the nanowire axis, we employ the gauge

$$A(\mathbf{r}) = B(0, 0, \Theta(\mathbf{r})), \tag{2a}$$

$$\Theta(\mathbf{r}) = y\cos\theta - x\sin\theta. \tag{2b}$$

Different orientations of the transverse field are obtained by the appropriate azimuthal angle θ, which is measured with respect to the x axis (see Fig. 1). $\theta = 0$ corresponds to a field oriented *along a maximal diameter* of the hexagonal core, while $\theta = 30°$ corresponds to a field which is *perpendicular to a facet* of the nanowire.

A uniform magnetic field in the transverse direction does not brake translational invariance along the wire axis, which is taken along the z direction [see Eq. (2)]. Therefore, the 3D electron envelope function $\Psi_n(\mathbf{R})$ can be factorized in a 1D plane wave and a 2D envelope function, $\Psi_{n,k}(\mathbf{R}) = e^{ikz}\phi_{n,k}(\mathbf{r})$, and labeled by the the principal quantum number, n, and the electron momentum along the z direction, k, with $\mathbf{r} = (x, y)$. By inserting $\Psi_{n,k}$ into the Hamiltonian, Eq. (1), the following equation for $\phi_{n,k}(\mathbf{r})$ is obtained:

$$\left\{-\frac{\hbar^2}{2}\nabla_{\mathbf{r}}\left[\frac{1}{m^*(\mathbf{r})}\nabla_{\mathbf{r}}\right] + \frac{1}{2}m^*(\mathbf{r})\omega_c(\mathbf{r})^2\left(\Theta(\mathbf{r}) - \Theta_0\right)^2 + E_C(\mathbf{r}) - e\,V(\mathbf{r})\right\}\phi_{n,k}(\mathbf{r}) = \epsilon_{n,k}\phi_{n,k}(\mathbf{r}). \tag{3}$$

Here, ω_c is the cyclotron frequency, $\omega_c(\mathbf{r}) = e\,B/m^*(\mathbf{r})$, and $\Theta_0 = k\,l_B^2$, with $l_B = \sqrt{\hbar/e\,B}$ being the magnetic length. Hence, in this gauge the transverse magnetic field amounts to an effective parabolic potential lying in the plane defined by the field direction and the normal to wire axis. Θ_0 is the vertex of the harmonic potential, which is displaced from the axis of the hexagonal section by $k\,l_B^2$ along the direction perpendicular to the field. This gauge is equivalent to the Landau gauge which in a planar Hall bar geometry gives rise to LLs in the bulk of the bar, and ESs near to the boundaries.[19] Here, however, there are no electrostatically defined edges, as in a Hall bar. In fact, lateral confinement in the direction perpendicular to the field results from charge redistribution in the complex three-dimensional structure, which has to be calculated self-consistently.

In zero magnetic field, subbands are parabolic, $\epsilon_{n,k} = \epsilon_n^0 + \hbar^2 k^2/2m^*$, with ϵ_n^0 the energy at $k = 0$, and $\phi_{n,k}(\mathbf{r})$ is k-independent. However, due to the presence of the magnetic term the subbands develop non trivial dispersions, strongly dependent on the self-consistent potential entering in Eq. (3), as we shall see in the next section. At the opposite limit of a large magnetic field, due to the non trivial localization of the electronic states, magnetic states can only partially be described in terms of the usual LLs and ESs.

We solve Eq. (3) for magnetic fields of arbitrary strength and orientation at several k-points on a uniform grid in $[-k_{max}, k_{max}]$, with k_{max} fairly above the Fermi wave vector. Then, the electron density is obtained from

$$n(\mathbf{r}) = 2 \sum_n \int_{-k_{max}}^{k_{max}} \frac{dk}{2\,\pi}\, f(\epsilon_{n,k} - \mu, T)\, |\phi_{n,k}(\mathbf{r})|^2 \,, \tag{4}$$

where the leading 2 on the right-hand-side accounts for spin degeneracy, and $f(\epsilon_{n,k} - \mu, T)$ is the Fermi occupation for each (k, n) state given by

$$f(\epsilon_{n,k}, \mu, T) = \frac{1}{1 + e^{(\epsilon_{n,k} - \mu)/k_B T}}, \tag{5}$$

μ, T and k_B being, respectively, the Fermi energy, temperature, and Boltzmann constant. The chemical potential μ is pinned by the surface states of the outer GaAs layer, and in our calculation is fixed exactly at midgap.

Once the electron density is determined, the Hartree electrostatic potential V_H due to the free charge and the ionized impurities is obtained from Poisson equation

$$\nabla \varepsilon(\mathbf{r}) \nabla V_H(\mathbf{r}) = \frac{1}{\varepsilon_0} e(n(\mathbf{r}) - \rho_D(\mathbf{r})). \tag{6}$$

Here, $\rho_D(\mathbf{r})$ is the volumetric density of dopants, which are considered to be fully ionized, while $\varepsilon(\mathbf{r})$ and ε_0 are the position-dependent dielectric constant and the vacuum permittivity. An exchange-correlation correction calculated within the local density approximation following a standard formulation[20,21] is also added to this electrostatic potential. Its contribution does not exceed few percent and does not give qualitative effects in the regimes addressed in the following.

Equations (3) to (7) are numerically integrated iteratively, with Dirichlet boundary conditions, through a box integration method on a triangular grid with hexagonal elements. The latter discretization, having the same symmetry of the integration domain, does not introduce numerical artifacts at the boundaries. No spatial symmetry is imposed, however. The original D_{6h} symmetry of the Hamiltonian is reduced to C_2 by the transverse field and no degeneracies are therefore to be obtained.

The whole procedure is iterated until self-consistency is reached, which we consider to occur at the particularly strict condition that the relative variation of the charge density between two consecutive iterations is lower than 0.001 at any point of the discretization domain. We refer the reader to Ref. 16 for more technical details about the numerical approach.

Once the convergence is achieved, energies and subbands occupations allow to estimate the ballistic conductance of the NW by means of the linear-response Landauer formula,

$$G = \frac{e^2}{h} \sum_n \int_{\mathcal{B}_n} -\frac{\partial f(E-\mu, T)}{\partial E}\, dE. \tag{7}$$

where the integral is performed on each (nonparabolic) energy band $\mathcal{B}_n$, from $E(-k_{max})$ to $E(k_{max})$, and gives a significant contribution only around the crossings of the band with the Fermy energy μ.

III. RESULTS AND DISCUSSION

Below we shall discuss magnetic states and magneto-conductance of the prototypical GaAs CSNW shown in Fig. 1 for different charge density regimes.[16] We shall find it important to differentiate between a magnetic field applied perpendicular to a facet and along a maximal diameter (joining two opposite vertices), since the anisotropic response to the field is a direct evidence of the inhomogeneous localization of the electron gas.

Our reference sample is a CSNW with a GaAs core having a facet-to-facet distance of 80 nm. The core is surrounded by a 50 nm thick $Al_{0.3}Ga_{0.7}As$ shell and a 10 nm thick GaAs capping layer. The system is n-doped with a constant density of donors ρ_D, uniformly distributed in a 10 nm thick layer, placed in the middle of the $Al_{0.3}Ga_{0.7}As$ shell. The

Fermi energy is pinned by GaAs surface states at the middle of the gap, and is taken as the reference level for energies, i.e. $\mu = 0$.

All calculations have been performed assuming a temperature of 4K. The position dependent material parameters employed in the calculations are $m^*(\mathrm{GaAs}) = 0.067$, $\varepsilon(\mathrm{GaAs}) = 13.8$, $E_c(\mathrm{GaAs}) = 0.715$ eV, and, $m^*(\mathrm{Al}_{0.3}\mathrm{Ga}_{0.7}\mathrm{As}) = 0.092$, $\varepsilon(\mathrm{Al}_{0.3}\mathrm{Ga}_{0.7}\mathrm{As}) = 12.24$, $E_c(\mathrm{Al}_{0.3}\mathrm{Ga}_{0.7}\mathrm{As}) = 0.999$ eV.

A. Magnetic states

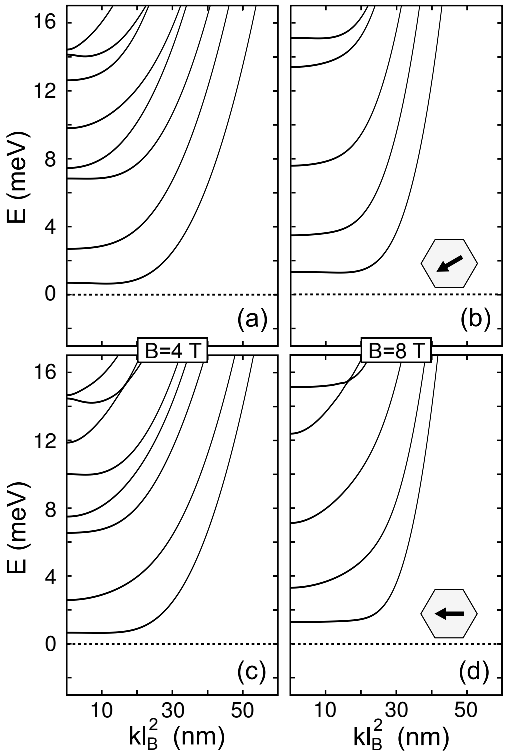

FIG. 2. Electron energy subbands vs the in-wire momentum k for a CSNW (see text) doped with $\rho_D = 1.44 \times 10^{18}\,\mathrm{cm}^{-3}$ under an external magnetic field. The horizontal dashed lines shows the Fermi energy position. Panels (a), (c): $B = 4\,\mathrm{T}$. Panels (b), (d): $B = 8\,\mathrm{T}$. Top panels: field oriented perpendicular to the facets. Bottom panels: field oriented along a diameter.

We start the discussion from the low doping-density regime, with $\rho_D = 1.44 \times 10^{18}$ cm^{-3}, which corresponds to a linear free-electron density 0.014×10^7 cm^{-1}, since this realizes, in a sense, the simplest situation. Figure 2 shows the subband dispersion in positive values of the in-wire momentum k (the dispersion in negative k is symmetric) at two representative values of the magnetic field, $B = 4\,\mathrm{T}$ (left) and $B = 8\,\mathrm{T}$ (right), and for the two orientations of the field. Note that the lowest subband edge lies slightly above the Fermi energy (dashed line), so that the self-consistent charge density, shown in Fig. 3, is determined by a fractional thermal occupation of the lowest subband only. The charge density (Fig. 3, top panel), which at zero field consists of a cylindrically symmetric quasi-1D channel extended over the GaAs core, is slightly distorted by the field and elongates in the direction normal to the field itself. This is a somewhat stronger effect with the field perpendicular to the facets, as in this configuration the lateral electrostatic confinement is wider.

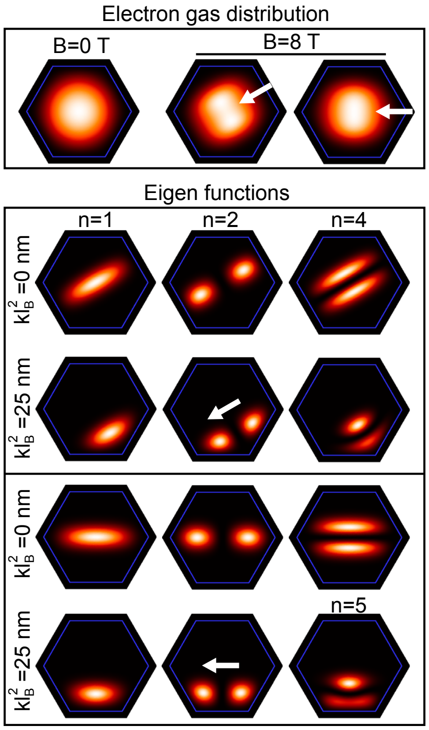

FIG. 3. Self-consistent charge density and envelope functions corresponding to electron states in Fig. 2. Top panel: 2D self-consistent charge density at zero magnetic field (left) and with $B = 8T$ (center and right), with the field oriented as shown by the arrows. Bottom panel: envelope functions squared at $B = 8\,\mathrm{T}$ for selected values of (n, k), as indicated by labels. In each row, the field is oriented as shown by the white arrow in the center/bottom map.

The overall dispersion of the lowest subbands in Fig. 2 strongly resembles the LLs/ESs picture, familiar from planar 2DEGs in a Hall bar geometry.[19] As the field is increased, the zero-field, parabolic dispersions at low k gradually flatten, and form highly degenerate bands, similarly to LLs. At the two representative fields shown in Fig. 2, the flat region extends for a wide k range, since the magnetic length l_B, which at 4 T and 8 T is $\sim 13\,\mathrm{nm}$ and $\sim 9\,\mathrm{nm}$, respectively, is much smaller than the lateral width of the states, which is of the order of the diameter of the GaAs core. At larger k, where kl_B^2 approaches the radius of the GaAs core, or, equivalently, the bottom of the magnetic harmonic potential approaches the lateral AlGaAs barriers by $\sim l_B$, the subbands become dispersed and bend up monotonously, similarly to ESs in a Hall bar.

The corresponding envelope functions are shown in the bottom panel of Fig. 3 for selected (n, k) values. At $k = 0$ electrons form LLs localized in the center of the structure, extending laterally, i.e., in the direction *orthogonal* to the field, by about l_B. States with zero ($n = 1, 2$) or one ($n = 4$) node in the *lateral direction* correspond to the first and second LL, respectively. At larger k (see $kl_B^2 = 25\mathrm{nm}$ Fig. 3) states are displaced laterally, and correspond to ESs in a standard Hall bar (states with negative k would be displaced in the opposite direction). Note that, depending on the field orientation, ESs localize either along a facet or an edge between two facets of the GaAs/AlGaAs interface.

The large thickness of the CSNW in the *vertical direction* (i.e. *along* the direction of the field) allows for several 1D subbands between successive LLs, like an electron gas in a wide quantum well.[22] For instance, in Fig. 2(b) the first three subbands correspond to the first LL ensuing from the lowest three in-wire subbands, with zero, one, or two nodal surfaces in the direction of the field (the former two are shown in Fig. 3 as $n = 1, 2$). These lowest subbands barely shift with the field [compare Figs. 2(a,b)], since their energy is mainly determined by the vertical confinement. On the other hand, the fourth subband corresponds to the second LL ensuing from the lowest subband, shown in Fig. 3 as $n = 4$, and has a nodal surface. Indeed, its energy do shift linearly with the field.

Despite the anisotropic, hexagonal spatial confinement, the subband dispersions for the two field orientations are similar, which is consistent with the almost isotropic self-consistent electron density at $B = 0$ shown in Fig. 3. The subbands in Figs. 2(c),(d) tend to be more dispersive than in Fig. 2(a),(b), since for the former field orientation, as k moves to large values, ESs are continuously squeezed by the converging AlGaAs barriers along the field direction (see Fig. 3). Note also that, for similar reasons, LLs ensuing from different subbands may have substantially different dispersions, and may cross at finite k, contrary to what happens in a large quantum well.

We next consider a CSNW with a slightly larger density of dopants, $\rho_D = 1.5 \times 10^{18}\,\mathrm{cm}^{-3}$, corresponding to a linear electron density $\approx 0.096 \times 10^{7}\,\mathrm{cm}^{-1}$, about seven times larger than in the previous case. The subband dispersions, and the self-consistent charge densities and envelope functions, are shown in Figs. 4 and 5, respectively, at the same two representative fields of the previous case. The zero field self-consistent charge density, shown in Fig. 5(top), consists of a hollow isotropic shell with finite thickness.[16] Therefore, it is expected that magnetic states resemble those of a cylindrical electron gas, which has been previously studied in the context of Carbon nanotubes[23] or cylindrical semiconductor systems.[24] Indeed, although the overall subband dispersion still resemble the LLs/ESs structure, the lowest subband is not monotonous. This type of dispersion is in agreement with single-particle calculations of the electron gas in the 2D surface of a cylinder.[24] The energy minimum corresponds to wavevectors such that electronic states may localize on the flanks of the structure, with respect to the magnetic field, i.e., in the regions where the normal component of the field vanishes. There, the residual vertical component of the field changes sign and, therefore, acts as a restoring force, keeping electrons confined to quasi-1D channels. Semiclassically, these correspond to twisting or oscillating orbits,[24,25] and add to the usual ESs or skipping orbits typical of planar structures.[26]

Having two density of states singularities in the lowest subband, one at $k = 0$ and one at a finite k, the Fermi energy is pinned to one of the two, depending on the field intensity. Note that the $k = 0$ states are localized on top or bottom of the structure with respect to the field direction, while states near to the minimum at $k \neq 0$ are localized on one side (which one depending on the sign of k). Accordingly, when the Fermi energy is pinned at $k = 0$ the charge density (not shown) is nearly isotropic and similar to the zero-field case, while when it is pinned at $k \neq 0$, the electron density is concentrated in two lobes parallel to the field direction, each being composed of states which are propagating in the direction of k or in the opposite direction.

The two lowest subbands are now nearly degenerate, since for this larger density the charge is pushed on opposite sides by the electron-electron interaction, similarly to a large quantum well,[22] forming a symmetric/anti-symmetric (SAS) pair (see Fig. 5, states with $n = 1, 2$). The pair is split in energy as k moves from $k = 0$ since, for these ESs, the vertical confinement is stronger and the tunneling energy correspondingly enhanced. Note also that, despite the apparent cylindrical symmetry at zero field, the response of the system

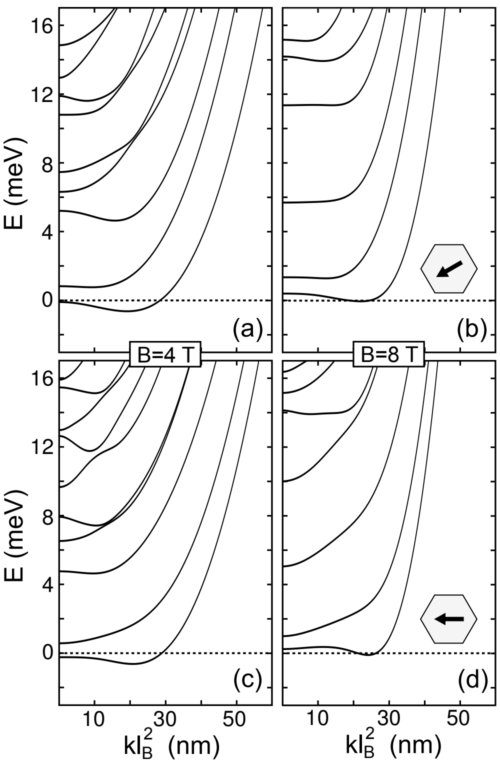

FIG. 4. Same as Fig. 2 for a NW doped with $\rho_D = 1.5 \times 10^{18}\,\mathrm{cm}^{-3}$.

to the magnetic field is somehow more anisotropic than in the previous, low density case, particularly for large fields and higher subbands, as can be seen comparing the top and bottom panels in Fig. 4.

Finally, we consider the case of a NW with a density of dopants $\rho_D = 1.7 \times 10^{18}\,\mathrm{cm}^{-3}$, corresponding to a linear electron density $0.425 \times 10^7\,\mathrm{cm}^{-1}$, about four times larger than the previous case. This is the more complex situation, but possibly the most relevant one from the point of view of high-mobility transport experiments. We show in Figs. 6 and 7 the subbands dispersion and the self-consistent charge distributions and envelope functions, respectively. Coulomb contribution is now dominating the Hamiltonian, and in this regime the zero field electron gas concentrates at the edges between two facets of the GaAs hexagonal core (Fig. 7, top-left panel) clearly exposing the $\mathrm{D_{6h}}$ symmetry of the CSNW. A transverse field further reduces the symmetry, but this is mainly observed in the envelope functions, while the self-consistent electron density is barely affected by the field.

The response of the system to the external magnetic field in this regime is appreciably anisotropic, due to the lower symmetry of the electron gas. Therefore, let us discuss sepa-

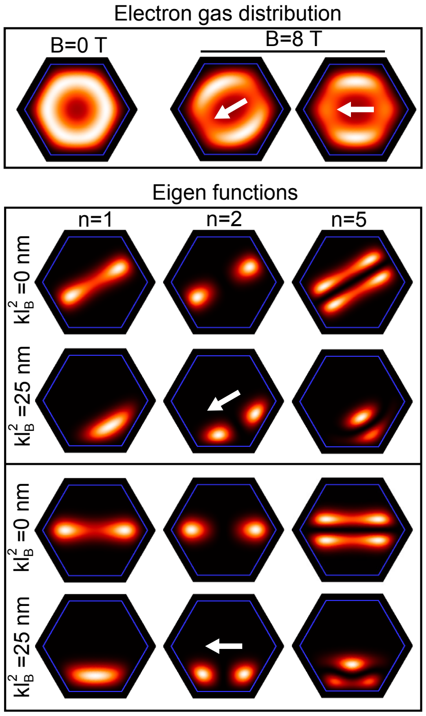

FIG. 5. Same as Fig. 3, but corresponding to electron states in Fig. 4.

rately the two field configurations, and first discuss the situation with the magnetic field applied perpendicularly to the facets. Because of the strong localization at the GaAs/AlGaAs interfaces, due to electron-electron interaction, the lowest subbands form a SAS pair which is nearly degenerate at small k (see Fig. 6). As the wavevector increases, both subbands bend down, corresponding to the formation of laterally confined states described also in the previous case, while SAS states with larger k split, since the magnetic fields confines the wave functions laterally. We show how this happens at the two representative fields 5 T and 15 T in Fig. 7, corresponding to Fermi energy pinning at the third subband and at the lowest SAS doublet, respectively. At the lower field, the situation is similar to lower densities, with LLs smoothly evolving in ESs through one minimum, because the magnetic confinement has a larger lengthscale than the electrostatic confinement at the edges. In contrast, at 15 T, although the states have a more flat dispersion, which is expected because of the larger field, they go through a double minimum. This is because at a specific k value the magnetic potential is centered exactly at the position of the self-consistent minima at the edges between the facets and with a similar confinement length (see $k\,l_B^2 = 16$ nm in Fig. 6). At larger k, ESs develop, as in the previous cases. The excited subbands still develop LL-like

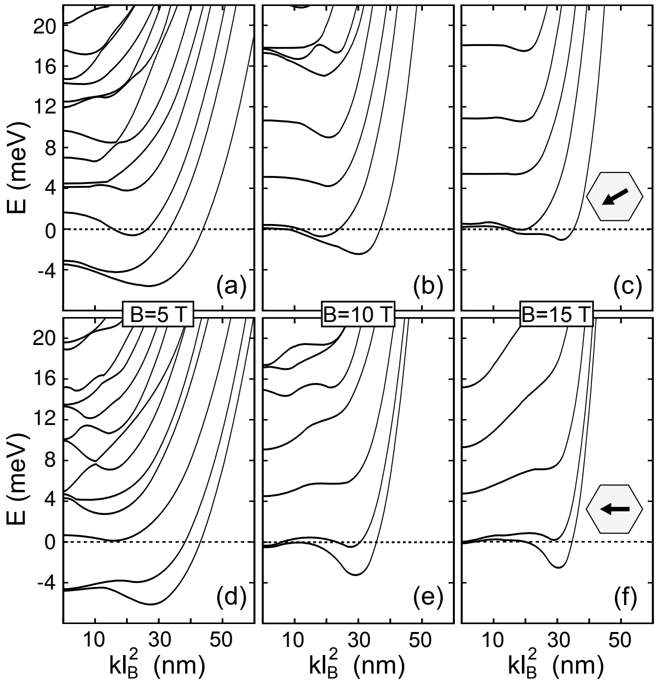

FIG. 6. Same as Fig. 2 with $\rho_D = 1.7 \times 10^{18}\,\mathrm{cm}^{-3}$. Panels (a), (d): $B = 5\,\mathrm{T}$. Panels (b), (e): $B = 10\,\mathrm{T}$. Panels (c), (f): $B = 15\,\mathrm{T}$.

flat band dispersion because they are spread over the center of the GaAs core, in a situation similar to the subbands illustrated in Fig. 2. Correspondingly, the magnetic field applied perpendicular to the facets slightly favors localization in the two edges along the orthogonal direction, but since the field adds to the strong self-consistent field here, this is only a minor effect (Fig. 7, top right).

We next consider a magnetic field applied in the direction of a maximal diameter of the hexagonal section. As shown in Fig. 6 (bottom panels), the flat band dispersion of a LL is now hardly observed even in higher bands, since for this orientation, as k increases the vertical (parallel to the field) spatial confinement decreases continuously (see Fig. 7, bottom panels). The two lowest subbands, which are nearly degenerate at $k = 0$, bend up with k and relax the degeneracy for the same reason, finally developing a minimum at finite k. The corresponding evolution of the wave functions with k is illustrated in the bottom panels of Fig. 7. At large field the dispersion is almost flat, until the states develop a minimum, which is much deeper than in the previous field orientation. Indeed, this corresponds to states which are delocalized along a facet.

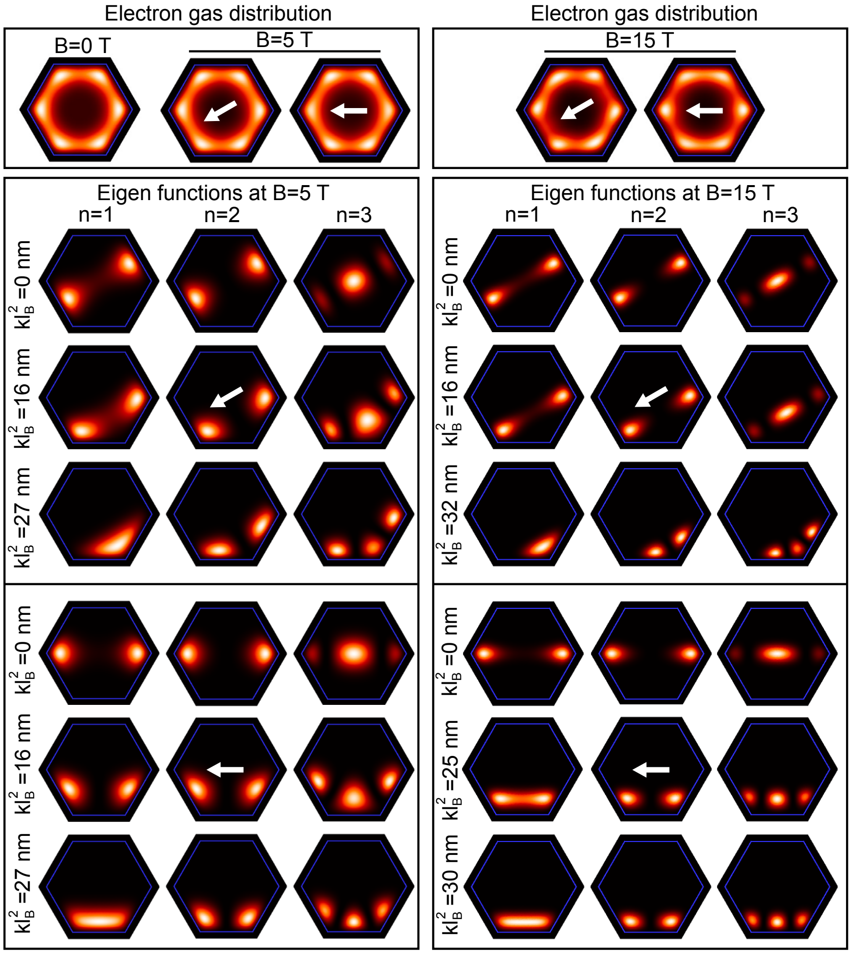

FIG. 7. Same as Fig. 3, but corresponding to electron states in Fig. 6. Charge density and envelope functions are shown for two fields, $B = 5$T (left panels), and $B = 15$T (right panels).

B. Density of states

In Fig. 8 we show the density of states of the NW with a density of dopants $\rho_D = 1.7 \times 10^{18}\,\mathrm{cm}^{-3}$ for both field orientations. LLs are easily identified at high fields as narrow peaks shifting linearly with the field. Since the Fermi energy is fixed by surface states at midgap, the lowest level is actually flat and pinned at the Fermi energy at sufficiently large field (correspondingly, as the field increases, the bottom of the self-consistent potential moves linearly at lower energies). Each LL comes as a set of parallel bands arising from the vertical confinement. However, the DOS cannot be described only in terms of highly degenerate LLs. This is exemplified by the two DOS profiles shown in Fig. 8 at selected magnetic fields, which show a rich structure on top of the LL peaks, which is due to the dispersive states localized on the flakes of the structure.[18] In particular, one can recognize high DOS below the lowest LL at intermediated fields.

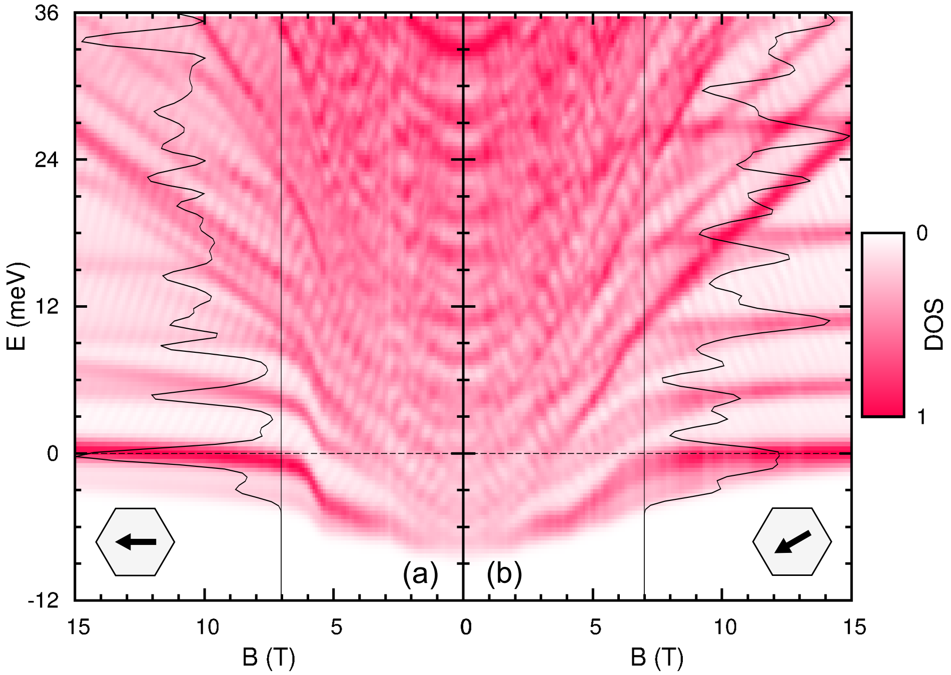

FIG. 8. Color intensity: normalized DOS vs transverse magnetic field intensity, with the field oriented as indicated in the insets. The Fermi energy is shown by a horizontal dashed line. In the left and right panels, a profile of the DOS at a specific field, indicated by a vertical line, is shown.

C. Magnetoconductance

To conclude this study, we focus on the behavior of the CSNW magneto-conductance, which may give direct experimental evidence of the localization of the electronic states. In a quasi-1D channel in the Quantum Hall regime the magnetoconductance decreases in steps of $2e^2/h$, corresponding to depletion of successive current carrying ESs which, in a planar geometry, emerge monotonously out of the highly degenerate LLs. We have shown above that CSNWs have a much more involved subband structure and DOS, which reflects itself in a peculiar magneto-conductivity behavior.

In Fig. 9(a) we show the calculated magneto-conductivity for the three doping densities considered before. For the two lowest doping densities G is low already at zero field due to the low free-carrier density of these systems. The magnetic field rapidly depletes the lowest level, which translates in a continuous reduction of the magnetoconductance. For the NW with the highest density of dopants, there are several occupied subbands at low fields, which are depleted by the field. Accordingly, magnetoconductance reduces up to $B \sim 6$ T, where it attains a minimum. At larger field, the conductance increases again, and finally falls to $G \simeq 2$ as the lowest state is depleted. Note that the negative magneto-resistance region exists for both orientations of the field, although it is more pronounced when the field is oriented along a maximal diameter. In the insets of Fig. 9(a) we illustrate the origin of the conductance behavior for this higher-density case. At $B = 4$T (left inset) there are four levels at the Fermi energy with a positive slope. At $B = 6$T (center inset) Fermi energy lies between the second and third subbands and only two channels are accessible, in a region with a low DOS (see Fig. 8). From here the conductance increases again, due to the non monotonous behavior of the two lowest subbands, which results in additional channels at higher field, as $B \sim 9$T (right inset). Note the anisotropy of the magnetoconductance with respect to the field orientation in proximity of the minimum (B_0) where, for fields oriented with the maximal diameter, G is lower than for the field normal to the facets as long as $B < B_0$, while the opposite is true for $B > B_0$. This anisotropy is highlighted in Fig. 9(b), where the conductance difference between the two field directions is reported as a percentage of their mean value. The change of sign of the anisotropy is therefore a clear signature of the different dispersions and inhomogeneous localization of the electron gas in CSNWs.

IV. CONCLUSIONS

Free-electron gas in CSNWs can expose characteristic properties of both one-dimensional and two-dimensional systems, depending on its localization, in the bulk core or at the prismatic heterointerface between different materials. These two regimes, not only add up but also show a complex interplay. In fact, in realistic conditions, both regimes are present and the appearance of different LLs and ESs can be tailored by a magnetic field orthogonal to the CSNW axis.

In this work, we simulated a realistic sample through a self-consistent mean field procedure and determined the following. First. Small variations of the doping density are able to modify the charge localization pattern from a 1D regime (electrons in the core) to a

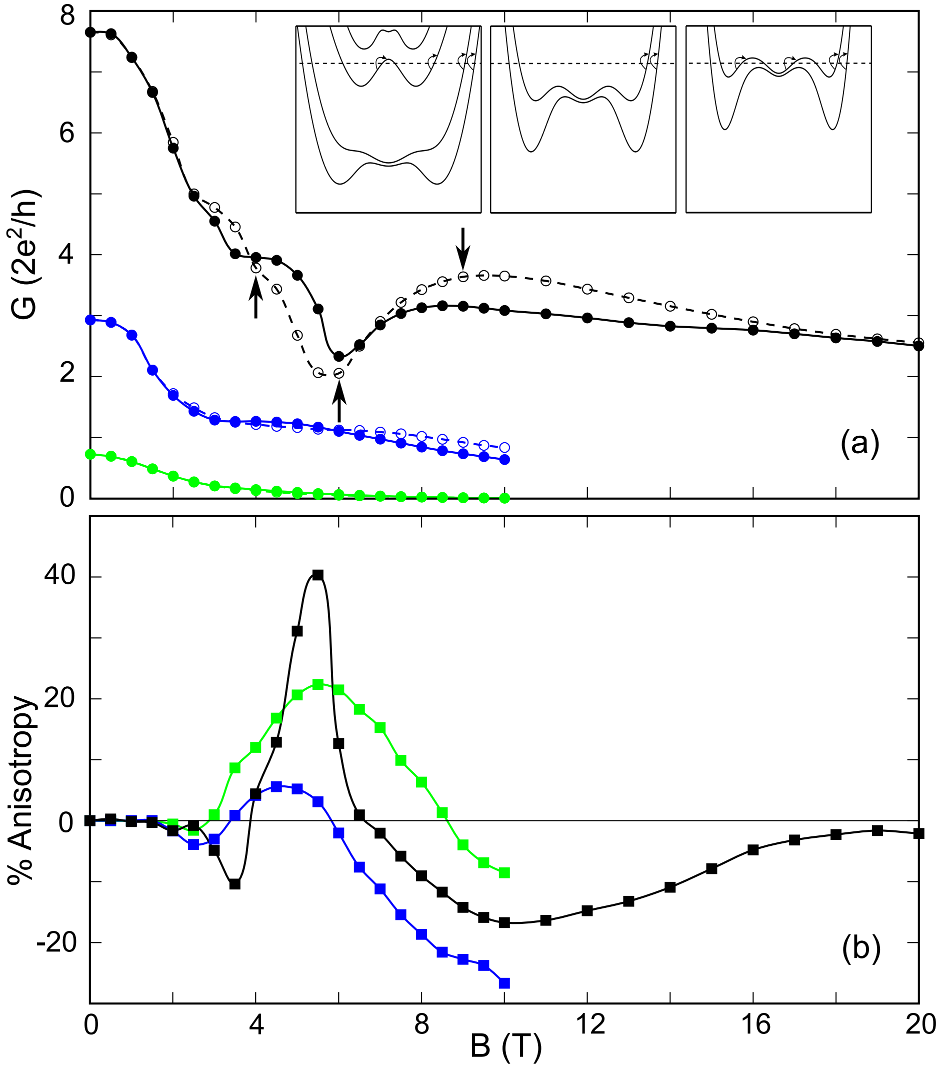

FIG. 9. Top panel. Magnetoconductance of the NW with three different doping densities: $\rho_D = 1.7 \times 10^{18}\,\mathrm{cm}^{-3}$ (upper black curve), $\rho_D = 1.5 \times 10^{18}\,\mathrm{cm}^{-3}$ (middle blue curve), and $\rho_D = 1.4 \times 10^{18}\,\mathrm{cm}^{-3}$ (lower green curve). Solid and dashed lines show the results for an orientation of the magnetic field along a maximal diameter and normal to a facet, respectively. The insets illustrate the subband structure and the intra-subband excitations responsible for the conductance at the three values of B indicated by the arrows of the main plot, in the same order. Bottom panel. Anisotropy of the magnetoconductance for the two directions of B. The higher density regime shows a pronounced anisotropy extending more than 60% between $B = 4$T and $B = 5$T. The circular/square points are the results of the simulations, while the connecting lines are an interpolation as guides to the eyes.

cylinder-like wrapped 2DEG (along the whole heterointerface) and to a set of six coupled

1D channels (at the vertices of the hexagonal section of the heterointerface). Second. The orthogonal magnetic field does not change much, at least qualitatively, the above localization patterns, but has a strong impact on the subband dispersions and on the density of states. Namely, novel minima at $k \neq 0$ appear, due to the competition between the magnetic length and the structure confinement. High density-of-states regions of the self-consistent subband structure pins to the Fermi level and a strong magnetic field enhances this effect due to the flattering of the bands at low k. Third. Electron-electron interaction leads to strongly inhomogeneous localization and is responsible for the stability of the 2DEG also in presence of strong magnetic fields. Fourth. The full inclusion of the prismatic cross-section in the numerical modeling of the CSNW is essential, since a cylindrical model, not taking into account the real sample symmetry, cannot reproduce the complex localization patterns and the different subband tailoring induced by the magnetic field. Fifth. A regime of negative magneto-resistance is predicted in the case with high doping density, contrary to the case of planar 2DEGs or purely 1D systems. Furthermore, a substantial anisotropy is present in the magnetoconductance, as the magnetic field is applied along the direction joining two opposite vertices or perpendicular to two opposite facets, this being a signature of the inhomogeneous localization of the electron gas.

---

[*] miguel.royovalls@unimore.it

[†] andrea.bertoni@nano.cnr.it

[‡] guido.goldoni@unimore.it

[1] A. Fontcuberta i Morral, D. Spirkoska, J. Arbiol, M. Heigoldt, J. R. Morante, and G. Abstreiter, Small **4**, 899 (2008).

[2] M. Keplinger, T. Martensson, J. Stangl, E. Wintersberger, B. Mandl, D. Kriegner, V. Holý, G. Bauer, K. Deppert, and L. Samuelson, Nano Letters **9**, 1877 (2009).

[3] M. Heigoldt, J. Arbiol, D. Spirkoska, J. M. Rebled, S. Conesa-Boj, G. Abstreiter, F. Peiro, J. R. Morante, and A. Fontcuberta i Morral, J. Mater. Chem. **19**, 840 (2009).

[4] K. Sladek, V. Klinger, J. Wensorra, M. Akabori, H. Hardtdegen, and D. Grützmacher, Journal of Crystal Growth **312**, 635 (2010).

[5] K. Storm, F. Halvardsson, M. Heurlin, D. Lindgren, A. Gustafsson, P. M. Wu, B. Monemar,

and L. Samuelson, Nature Nanotechnology **7**, 718 (2012).

[6] C. M. Lieber and Z. L. Wang, MRS Bulletin **32**, 99 (2007).

[7] See, e.g, IEEE Journal of Selected Topics in Quantum Electronics, **17** (2012) for a recent collection of papers on the topic.

[8] H. Shtrikman, R. Popovitz-Biro, A. Kretinin, and M. Heiblum, Nano Lett. **9**, 215 (2009).

[9] H. Shtrikman, R. Popovitz-Biro, A. Kretinin, L. Houben, M. Heiblum, M. Bukała, M. Galicka, R. Buczko, and P. Kacman, Nano Lett. **9**, 1506 (2009).

[10] K. Tomioka, J. Motohisa, S. Hara, K. Hiruma, and T. Fukui, Nano Lett. **10**, 1639 (2010).

[11] N. Jiang, P. Parkinson, Q. Gao, S. Breuer, H. H. Tan, J. Wong-Leung, and C. Jagadish, App. Phys. Lett. **101**, 023111 (2012).

[12] K. Tomioka, M. Yoshimura, and T. Fukui, Nature **488**, 189 (2012).

[13] D. Spirkoska, G. Abstreiter, and A. F. I. Morral, Semicond. Sci. Technol. **24**, 113001 (2009).

[14] D. Spirkoska, A. F. i Morral, J. Dufouleur, Q. Xie, and G. Abstreiter, Phys. Status Solidi RRL **5**, 353 (2011).

[15] A. Li, D. Ercolani, L. Lugani, L. Nasi, F. Rossi, G. Salviati, F. Beltram, and L. Sorba, Crys. Growth & Design **11**, 4053 (2011).

[16] A. Bertoni, M. Royo, F. Mahawish, and G. Goldoni, Phys. Rev. B **84**, 205323 (2011).

[17] B. M. Wong, F. Leonard, Q. Li, and G. T. Wang, Nano Letters **11**, 3074 (2011).

[18] G. Ferrari, G. Goldoni, A. Bertoni, G. Cuoghi, and E. Molinari, Nano Letters **9**, 1631 (2009).

[19] A. H. MacDonald and P. Streda, Phys. Rev. B **29**, 1616 (1984).

[20] O. Gunnarsson and B. I. Lundqvist, Phys. Rev. B **13**, 4274 (1976).

[21] T. Ando, H. Taniyama, N. Ohtani, M. Nakayama, and M. Hosoda, J. Appl. Phys. **94**, 4489 (2003).

[22] D. G. Hayes, M. S. Skolnick, D. M. Whittaker, P. E. Simmonds, L. L. Taylor, S. J. Bass, and L. Eaves, Phys. Rev. B **44**, 3436 (1991).

[23] H. Ajiki and T. Ando, J. Phys. Soc. Jpn. **62**, 1255 (1993).

[24] G. Ferrari, A. Bertoni, G. Goldoni, and E. Molinari, Phys. Rev. B **78**, 115326 (2008).

[25] S. Bellucci and P. Onorato, Phys. Rev. B **82**, 205305 (2010).

[26] C. W. J. Beenakker, H. Van Houten, and B. J. Vanwees, Superlat. Microstruct. **5**, 127 (1988).